Seeded growth of large single-crystal copper foils with high-index facets

https://doi.org/10.1038/s41586-020-2298-5

Received: 29 March 2019

Accepted: 11 March 2020

Published online: 27 May 2020


Check for updates

Muhong Wu[1,2,3,16], Zhibin Zhang[1,16], Xiaozhi Xu[4,16], Zhihong Zhang[2,16], Yunrui Duan[5,6], Jichen Dong[5], Ruixi Qiao[2], Sifan You[2], Li Wang[1,7], Jiajie Qi[1], Dingxin Zou[8], Nianze Shang[1], Yubo Yang[9], Hui Li[6], Lan Zhu[10], Junliang Sun[11], Haijun Yu[9], Peng Gao[2], Xuedong Bai[7], Ying Jiang[2,12], Zhu-Jun Wang[13], Feng Ding[5,14]✉, Dapeng Yu[8]✉, Enge Wang[2,3,15]✉ & Kaihui Liu[1,2]✉

The production of large single-crystal metal foils with various facet indices has long been a pursuit in materials science owing to their potential applications in crystal epitaxy, catalysis, electronics and thermal engineering[1–5]. For a given metal, there are only three sets of low-index facets ({100}, {110} and {111}). In comparison, high-index facets are in principle infinite and could afford richer surface structures and properties. However, the controlled preparation of single-crystal foils with high-index facets is challenging, because they are neither thermodynamically[6,7] nor kinetically[3] favourable compared to low-index facets[6–18]. Here we report a seeded growth technique for building a library of single-crystal copper foils with sizes of about 30 × 20 square centimetres and more than 30 kinds of facet. A mild pre-oxidation of polycrystalline copper foils, followed by annealing in a reducing atmosphere, leads to the growth of high-index copper facets that cover almost the entire foil and have the potential of growing to lengths of several metres. The creation of oxide surface layers on our foils means that surface energy minimization is not a key determinant of facet selection for growth, as is usually the case. Instead, facet selection is dictated randomly by the facet of the largest grain (irrespective of its surface energy), which consumes smaller grains and eliminates grain boundaries. Our high-index foils can be used as seeds for the growth of other Cu foils along either the in-plane or the out-of-plane direction. We show that this technique is also applicable to the growth of high-index single-crystal nickel foils, and we explore the possibility of using our high-index copper foils as substrates for the epitaxial growth of two-dimensional materials. Other applications are expected in selective catalysis, low-impedance electrical conduction and heat dissipation.

At present, high-index metal foils are mainly obtained by cutting bulk single-crystal metal ingots or by epitaxial deposition on other non-metal single crystals with a high-index facet[19,20]. Thus, only a few index choices are available, and the cost is very high. Additionally, in the typical cutting and polishing method, accurate index control and flat surfaces with uniformly parallel step edges are very challenging to realize (with typically a 1°–3° tolerance in the cutting angle of single crystals from commercial products). Hence, new methods that enable efficient production of large single-crystal metal foils with various high-index facets are in great demand.

Recently, the synthesis of noble metal nanocrystals with high-index facets by electrochemical reaction, electrodeposition or solution-phase synthesis has been reported[3,4]. The basic idea in high-index noble metal nanocrystal growth is to perturb the thermodynamic equilibrium state of a low-index facet or to modify the kinetic barrier to the growth of a high-index seed. In our experiment, we first developed a pre-oxidation treatment technique to generate a large grain seed with a high-index facet in a commercial polycrystalline Cu foil. The Cu foils were oxidized at 150–650 °C in air, typically for a few hours, and then annealed in a reducing atmosphere at 1,020 °C for

[1]State Key Laboratory for Mesoscopic Physics, Frontiers Science Center for Nano-optoelectronics, School of Physics, Peking University, Beijing, China. [2]International Center for Quantum Materials, Collaborative Innovation Center of Quantum Matter, Peking University, Beijing, China. [3]Songshan Lake Materials Laboratory, Institute of Physics, Chinese Academy of Sciences, Guangdong, China. [4]Guangdong Provincial Key Laboratory of Quantum Engineering and Quantum Materials, School of Physics and Telecommunication Engineering, South China Normal University, Guangzhou, China. [5]Centre for Multidimensional Carbon Materials, Institute for Basic Science, Ulsan, South Korea. [6]Key Laboratory for Liquid–Solid Structural Evolution and Processing of Materials, Ministry of Education, Shandong University, Jinan, China. [7]Beijing National Laboratory for Condensed Matter Physics, Institute of Physics, Chinese Academy of Sciences, Beijing, China. [8]Shenzhen Institute for Quantum Science and Engineering, and Department of Physics, Southern University of Science and Technology, Shenzhen, China. [9]College of Materials Science and Engineering, Beijing University of Technology, Beijing, China. [10]Peking Union Medical College Hospital, Beijing, China. [11]College of Chemistry and Molecular Engineering, Peking University, Beijing, China. [12]Physical Science Laboratory, Huairou National Comprehensive Science Centre, Beijing, China. [13]Scientific Centre for Optical and Electron Microscopy, Eidgenössische Technische Hochschule Zürich, Zurich, Switzerland. [14]School of Materials Science and Engineering, Ulsan National Institute of Science and Technology, Ulsan, South Korea. [15]School of Physics, Liaoning University, Shenyang, China. [16]These authors contributed equally: Muhong Wu, Zhibin Zhang, Xiaozhi Xu, Zhihong Zhang. ✉e-mail: f.ding@unist.ac.kr; yudp@sustc.edu.cn; egwang@pku.edu.cn; khliu@pku.edu.cn

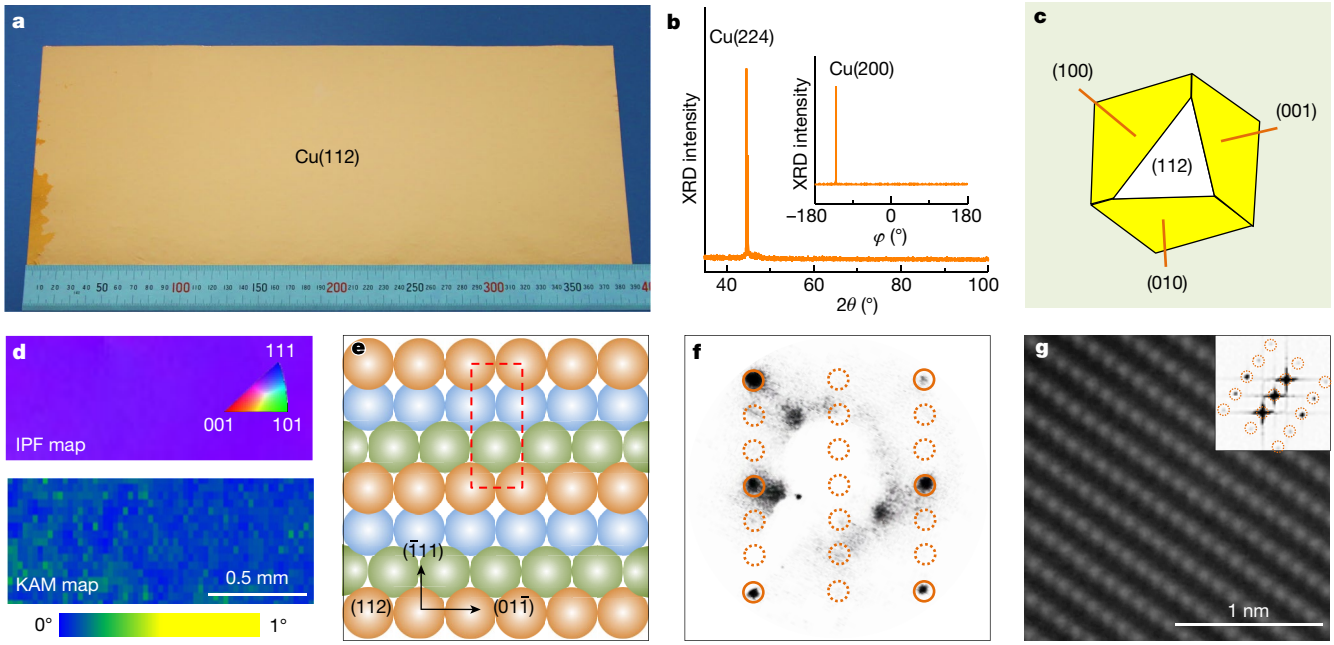

Fig. 1 | Characterization of a Cu(112) single crystal annealed from a commercial polycrystalline foil. a, Optical image of a single-crystal Cu(112) after mild oxidation in air at 200 °C. The single-crystal Cu(112) shows a homogeneous colour (the small darker pattern at the bottom-left corner is the polycrystalline part). The foil size is 39 × 21 cm^2. The rulers shown in all figures indicate millimetres unless stated otherwise. **b**, XRD 2θ scan data for the annealed Cu foil with (224) or (112) orientation. Inset, azimuthal off-axis φ scan spectrum with only one peak corresponding to Cu(200), confirming single-crystal features without in-plane rotation. **c**, Reconstructed single-crystal XRD pattern of the Cu(112) foil. **d**, Representative IPF (top) and KAM (bottom) maps of a Cu(112) foil. **e**, Schematic diagram of the Cu(112) surface. The orange, green and blue balls correspond to the first, second and third layers of Cu atoms from the surface, respectively. The red dashed box indicates the primitive cell for the first layer of Cu(112). **f**, Representative LEED pattern of the as-prepared Cu(112) foil. **g**, Atomically resolved STEM image of the Cu(112) foil. Inset, fast Fourier transform pattern of the STEM image.

several hours (see Methods for more details). The as-annealed Cu foil was heated in air at about 200 °C for 2–30 min before optical imaging. Owing to the difference in oxidation barriers, different types of facets show distinct colours, and a single-crystal Cu domain can be clearly observed as a homogeneous region in an optical image[21]. After thermal annealing, the whole ~39 × 21 cm^2 commercial polycrystalline Cu foil was transformed into a large single crystal (see Fig. 1a, where only the small dark orange zone at the bottom-left corner is polycrystalline), which is the largest single-crystal Cu foil reported so far, to our knowledge. This appealing property is enabled by our large annealing furnace, with a heating area of length 50 cm and diameter 23 cm, which provides a highly stable temperature distribution. The X-ray diffraction (XRD) 2θ scan (Fig. 1b) reveals that after pre-oxidation and subsequent annealing, the facet of the single crystal is not Cu(111), as reported before[12–14], but Cu(224) or Cu(112) (only facets with all Miller indices h, k and l even or odd give a non-zero 2θ scan signal in XRD owing to the extinction rule). A further azimuthal off-axis φ scan shows only one peak corresponding to Cu(200) (inset in Fig. 1b), demonstrating that the as-annealed Cu foil is a single crystal without in-plane rotation. To further confirm its crystal structure, single-crystal XRD was performed, and lattice reconstruction using a standard procedure confirms the (112) facet (Fig. 1c). Electron back-scattered diffraction (EBSD) was also applied to analyse the surface crystallography. The uniform violet colour in the inverse pole figure (IPF) map verifies the (112) facet index (top panel in Fig. 1d); the kernel average misorientation (KAM) map (bottom panel in Fig. 1d) shows that the local average misorientation between each measured point and its nearest neighbours is extremely small (typically less than 0.3°), indicating that the as-annealed Cu foil is a homogeneous single crystal. The (112) lattice structure of the as-annealed Cu (schematic in Fig. 1e) was also demonstrated in both reciprocal space and real space by low-energy electron diffraction (LEED; Fig. 1f) and scanning transmission electron microscopy (STEM; Fig. 1g), respectively.

With our design, the Cu(111) facet is no longer the only thermodynamically favourable facet, and a high-index facet, such as Cu(112), can be successfully synthesized. We repeated the procedure on many Cu foils, and more than 30 kinds of high-index single crystal with large domain sizes were prepared (length 25–39 cm, width 21 cm). Eight representative kinds of Cu foil with different facet indices and a typical size of 35 × 21 cm^2 are shown in Fig. 2a (the large uniform regions are single crystals). The single-crystal nature of the annealed Cu foils was further confirmed by the distinct colours in the corresponding EBSD IPF maps (Fig. 2b). The facet indices were identified by the characteristic peaks in the XRD 2θ scan spectra (Fig. 2c) and reconstructed single-crystal XRD data (Extended Data Fig. 1). Some high-index surface structures were further revealed by atom-resolved scanning tunnelling microscopy (STM) images (Extended Data Fig. 2), in which the spacing between atomic stripes matches the theoretical values from the atomic model.

To verify the essential role of the pre-oxidation treatment in producing high-index facets (Fig. 3a, stage 1), we carried out a control experiment in which we locally oxidized one end of a piece of polycrystalline Cu foil while the other end remained intact (Fig. 3b). After the annealing procedure, the pre-oxidized part was transformed into Cu(235) and the untreated part was transformed into Cu(111) (Fig. 3c, Extended Data Fig. 3). Statistical data further revealed that only Cu(111) foils were obtained without pre-oxidation; when the Cu foils were pre-oxidized, more than 30 types of facet were observed (Fig. 3d, e, Extended Data Table 1).

The above observations clearly reveal that pre-oxidation must induce some critical factor that controls the formation of high-index seeds. It is well established that the stored strain energy and the surface energy in a thin metal film are competitive driving forces for abnormal grain growth during annealing, with the former leading to abnormal Cu(001) grains because the smallest biaxial modulus of Cu is along the ⟨001⟩ direction[9], and the latter giving the facet with the minimum surface energy. Before the start of the abnormal grain growth, our thin (only

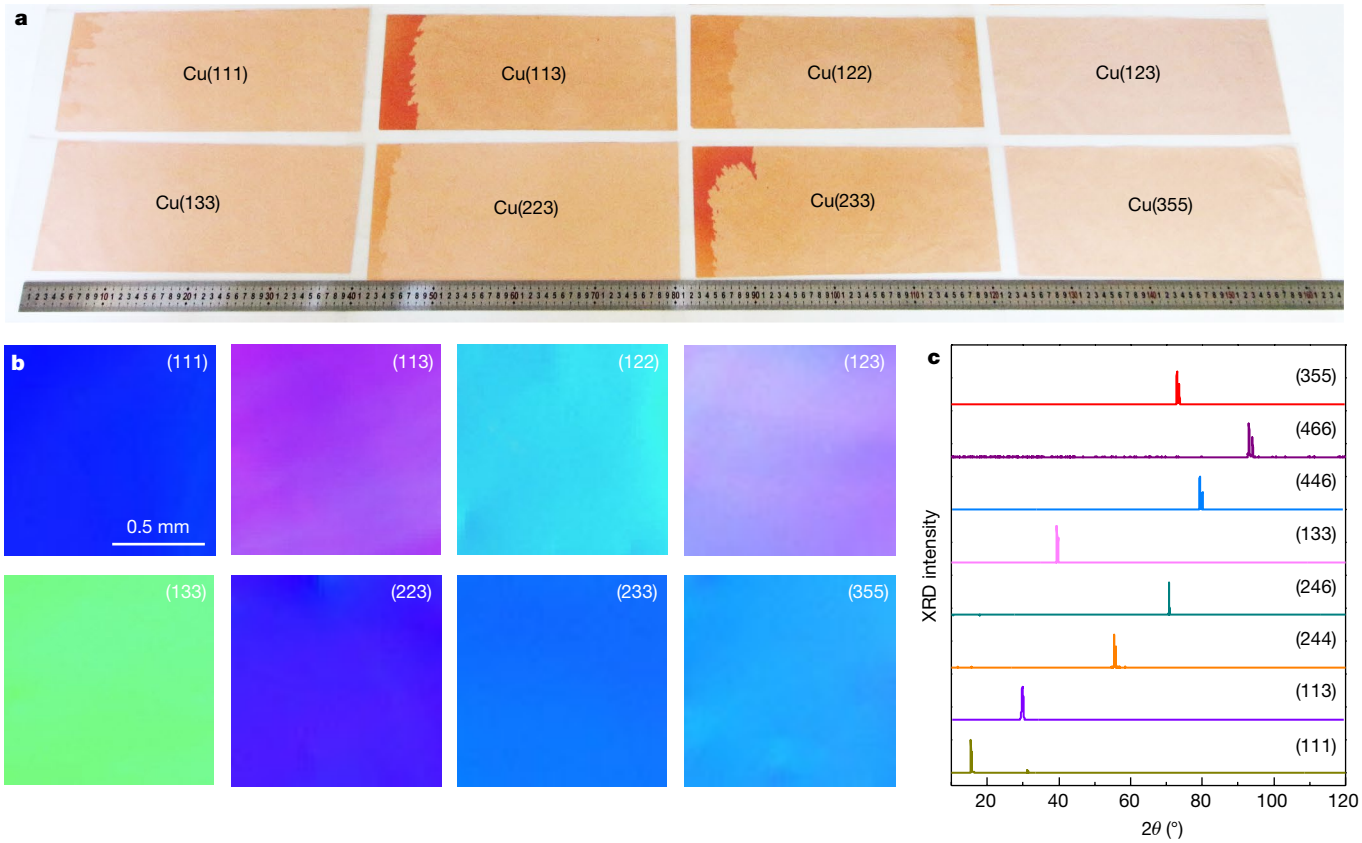

Fig. 2 | Single-crystal Cu foils of A4 paper size with various facet indices. **a**, Optical image of the eight representative types of single-crystal Cu foil with typical size of 35 × 21 cm^2. A mild oxidation treatment was performed to quickly identify the single-crystal region in the foils (the uniform areas are single crystals; the coloured corners are polycrystalline). The ruler indicates centimetres. **b**, EBSD IPF maps of the eight kinds of single-crystal Cu foil. The distinct colours reveal their different facet indices. These maps have the same size. **c**, XRD 2θ scan spectra of the eight kinds of single-crystal Cu foil. The characteristic peaks are used to identify the facet indices (owing to the extinction rule in XRD, only peaks corresponding to (244), (246), (446) and (466) appear, respectively, for the (122), (123), (223) and (233) facets). The X-ray source is a silver-based target with wavelength of about 0.56 Å and all the peaks are normalized with respect to the intensity maximum.

25 μm thick) Cu foil was annealed at 1,020 °C for a long time; thus, most of the stored strain energy was released, and the abnormal grain growth was mainly driven by the surface energy. As a consequence, annealing of an original Cu foil results in a Cu(111) single crystal with the lowest surface energy among all possible facets[12–14].

On the other hand, when Cu is mildly oxidized, both of its upper and lower surfaces are covered by a layer of Cu_xO grains with different orientations (Extended Data Fig. 4). Thus, the two free surfaces of a Cu grain are transformed into two Cu–Cu_xO interfaces after pre-oxidation, and then the interface energy, which is the summation of the energies of all types of interfaces between many small polycrystalline Cu_xO grains and the Cu foil, depends weakly on the orientation of the Cu grain itself. Therefore, grain seeds with various surface indices (Cu(*hkl*)) have certain probabilities of growing abnormally until the oxide layer is completely reduced. With further annealing, the Cu(*hkl*) grain seed with an advantage in size spreads to the whole Cu foil by abnormal grain growth (Fig. 3b, stage 2).

Unlike abnormal grain seeding, which is mainly driven by thermodynamics, abnormal grain growth is mainly controlled by kinetics. The large abnormal grain consumes the surrounding small normal grains and eliminates the grain boundaries in the Cu foil. In such a process, excessive oxygen at the grain boundaries acts as pinning centres and lowers the mobility of the grain boundaries[22]. Introducing hydrogen during annealing removes excessive oxygen from the Cu foil and accelerates the abnormal grain growth. In addition, the designed in-plane temperature difference throughout the Cu foil facilitates only one abnormal grain acting as a seed in the high-temperature region in most annealing processes (Extended Data Fig. 5). We also notice that the surface energy of pure Cu may play some role during the abnormal grain growth, favouring the formation of low-energy facets, because some parts of the oxide layer could be reduced to Cu during the annealing in the abnormal grain seeding stage[23–30] (Fig. 3f, Extended Data Table 1).

Using this technique, we can readily obtain large single-crystal Cu foils with various high-index facets. However, the appearance of a certain high-index seed is a random event and cannot be experimentally designed. To controllably produce the desired high-index single-crystal Cu foils, we further propose a facet 'transfer' method to copy the facet of the obtained high-index single crystals. First, a small piece of high-index single-crystal Cu, cut from a large single-crystal Cu foil obtained by pre-oxidation annealing, was placed on a large polycrystalline Cu foil to serve as a new seed. When annealed at a high temperature (but below the melting point of the bulk Cu), the surface of the seed started to assimilate into the polycrystalline Cu, and the single-crystal lattice arrangement had a very high chance (>98% under our current experimental conditions) of transferring to the polycrystalline Cu, resulting in a 'nucleus' with the same facet as the seed (Extended Data Fig. 6a). The time evolution of the thermal annealing process verifies that the facet 'transfer' indeed works, as shown by the example Cu(245) single crystal. The triangular single-crystal Cu(245) piece first assimilated from the top surface, on which the seed was placed, to the bottom surface of the polycrystalline Cu foil (Fig. 4a, b), and a new Cu(245) seed was formed in the polycrystalline foil that then spread into a large single crystal (Fig. 4c, d). The identical colour of the EBSD IPF maps (Fig. 4e), together with the XRD 2θ and φ scan data for the initial seed

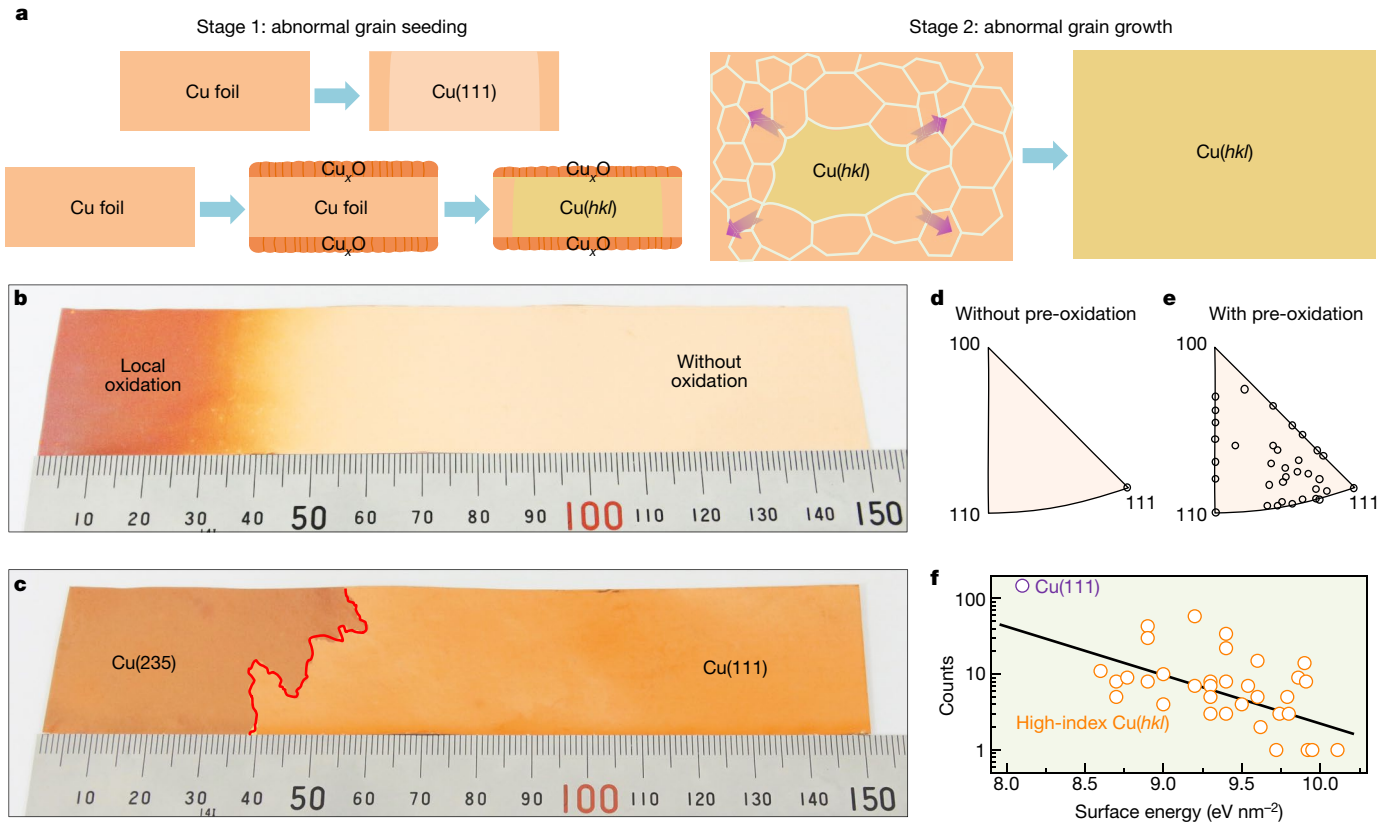

Fig. 3 | Pre-oxidation-guided seeded growth of single-crystal Cu foils with high facet indices. a, Schematic diagrams of the two stages of the fabrication of high-index single crystals. Stage 1: without an oxide layer, Cu(111) has the lowest surface energy and is the prevailing growing facet. Once the oxide layer is formed, high-index Cu(*hkl*) can grow, and form the abnormal grain seed. Stage 2: the large abnormal grain seed consumes the surrounding small normal grains and eliminates the grain boundaries in the Cu foil. **b**, **c**, Optical images of a Cu foil before (**b**) and after (**c**) annealing. One terminal of the Cu foil was pre-oxidized locally and the other one was kept intact before annealing. After annealing, the pre-oxidized terminal transformed into Cu(235) and the intact one changed into Cu(111). **d**, **e**, IPFs in the normal direction for the distribution of facet indices of Cu single crystals annealed without (**d**) and with (**e**) pre-oxidation. 35 kinds of Cu facet appeared with the pre-oxidation treatment, in striking contrast to the occurrence of only the Cu(111) facet without pre-oxidation. **f**, Appearance frequency of facets as a function of their surface energy for the single-crystal Cu foils obtained. The general trend shows that facets with lower surface energies can be achieved more easily. All the samples were pre-oxidized under the same conditions (150 °C for 2 h) and had almost the same oxide thickness (~50 nm).

and the final obtained Cu (Extended Data Fig. 6b–f), showed that the facet of the seed was successfully copied and a new large-size Cu(245) single crystal was produced. In addition to this in-plane facet transfer, we also found that a Cu foil can be transformed into 'bulk' single-crystal Cu by an out-of-plane facet transfer process, as shown in Fig. 4f. Here, the length of each foil was deliberately increased by about 2 mm with respect to the previous one to facilitate characterization of the obtained single crystal. The identical colour of the EBSD IPF maps for the different layers of Cu foils after cyclic facet 'transfer', together with the XRD characterization for the whole thick Cu foil, demonstrated that the single-crystal structure of the first Cu(256) layer was successfully transferred throughout the foil (Fig. 4g–i, Extended Data Fig. 6g), revealing a new facile way to prepare a bulk single-crystal Cu slab with controlled crystal orientation. The above processes of vertical assimilation and in-plane growth were explained and reproduced by our molecular dynamics simulations (Extended Data Fig. 7).

To demonstrate the universality of this seeded abnormal grain growth technique, we attempted to anneal nickel (Ni) using a similar approach at about 1,200 °C. Three types of high-index single-crystal Ni foil with (012), (013) and (355) facets, typically with a size of about 5 × 5 cm^2, were obtained (Fig. 4j–n, Extended Data Fig. 8). The Ni single-crystal size was limited by the diameter of the alundum tubes in our custom-designed high-temperature chemical vapour deposition system. In addition to Cu and Ni, we expect that similar approaches could be applied to grow single-crystal foils of many other metals (such as Fe, Al, Ag and Pt) and their alloys. Moreover, we found that the epitaxial growth of graphene and hexagonal boron nitride (hBN) is also achievable on high-index facets (Extended Data Fig. 9), not only on Cu(111) (refs. [12,13]) or vicinal Cu(110) (ref. [18]), as previously reported. We therefore expect further advancement in the fundamental exploration and technical applications of these large high-index single-crystal metal foils.

Online content

Any methods, additional references, Nature Research reporting summaries, source data, extended data, supplementary information, acknowledgements, peer review information; details of author contributions and competing interests; and statements of data and code availability are available at https://doi.org/10.1038/s41586-020-2298-5.

1. Lin, C. et al. Two-dimensional wetting of a stepped copper surface. *Phys. Rev. Lett.* **120**, 076101 (2018).
2. Park, C. H. et al. Anisotropic behaviours of massless Dirac fermions in graphene under periodic potentials. *Nat. Phys.* **4**, 213–217 (2008).
3. Tian, N. et al. Synthesis of tetrahexahedral platinum nanocrystals with high-index facets and high electro-oxidation activity. *Science* **316**, 732–735 (2007).
4. Quan, Z. W., Wang, Y. X. & Fang, J. Y. High-index faceted noble metal nanocrystals. *Acc. Chem. Res.* **46**, 191–202 (2013).
5. Huang, X. et al. Solution-phase epitaxial growth of noble metal nanostructures on dispersible single-layer molybdenum disulfide nanosheets. *Nat. Commun.* **4**, 1444 (2013).

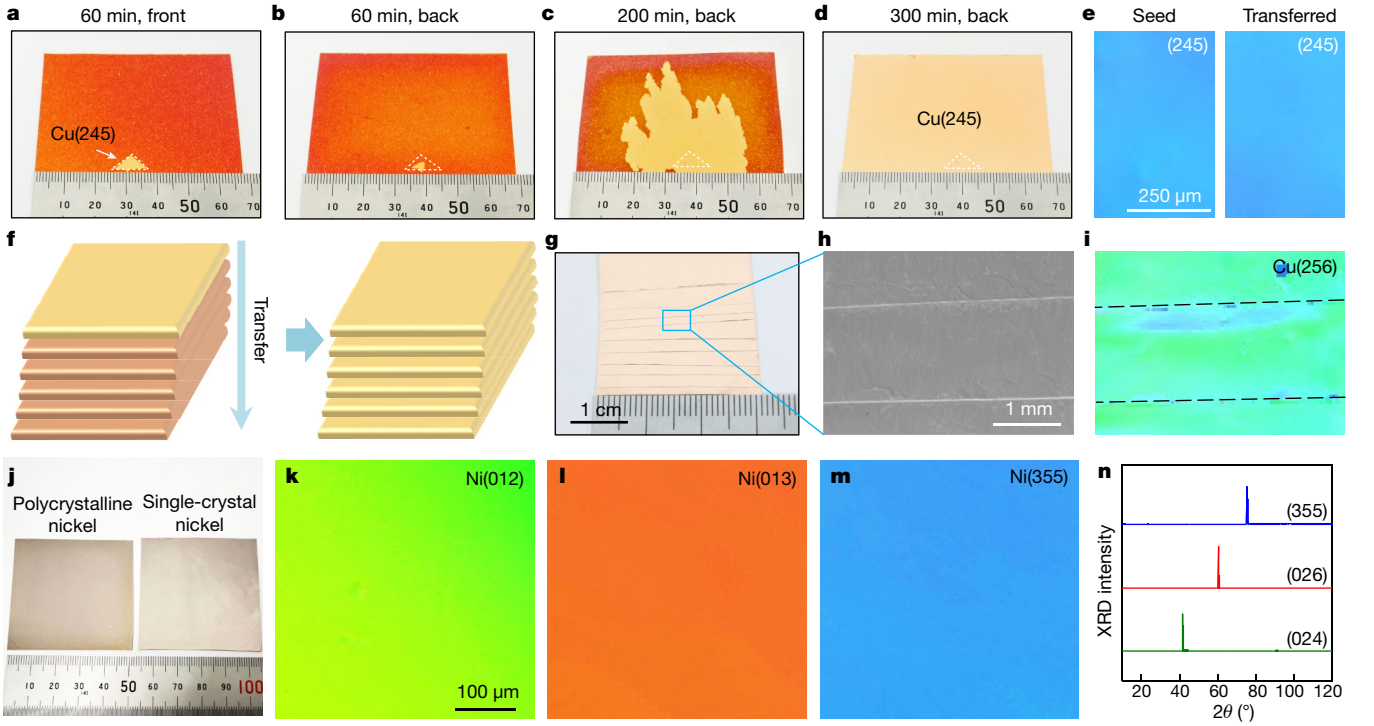

Fig. 4 | Facet transfer of single-crystal Cu and characterization of high-index single-crystal Ni foils. a, Photograph of the front surface of a Cu foil after seed-guided annealing for 60 min. **b**–**d**, Photographs of the back surfaces of Cu foils after seed-guided annealing for 60 min (**b**), 200 min (**c**) and 300 min (**d**). **e**, EBSD IPF maps of the seed (left) and the Cu single crystals with the transferred facet (right). The identical colour shows that the (245) single-crystal structure was copied successfully. The two EBSD maps have the same size. The facet index is determined from the XRD characterization in Extended Data Fig. 6b–f. **f**, Schematic diagrams illustrating out-of-plane facet transfer layer by layer. **g**, Optical image of the ten layers of Cu foils with transferred facets. The length of the foils was deliberately increased by ~2 mm each time to facilitate the sample characterization. **h**, **i**, SEM image (**h**) and EBSD IPF map (**i**) of the Cu foils marked in **g**. The uniform colour in the EBSD IPF map, together with the XRD data in Extended Data Fig. 6g, demonstrates that the single-crystal structure of the first Cu layer has been successfully copied by all the foils in the slab. **j**, Photograph of polycrystalline (left) and single-crystal (right) Ni foils with size of about 5 × 5 cm^2. **k**–**m**, EBSD IPF maps of three kinds of single-crystal Ni foil. The distinct colours reveal their different facet indices. These maps are of the same size. **n**, Powder XRD (silver-based target) 2θ scan spectra of the single-crystal Ni foils shown in **k**–**m**.

6. Vitos, L., Ruban, A. V., Skriver, H. L. & Kollar, J. The surface energy of metals. *Surf. Sci.* **411**, 186–202 (1998).
7. Wen, Y. N. & Zhang, H. M. Surface energy calculation of the fcc metals by using the MAEAM. *Solid State Commun.* **144**, 163–167 (2007).
8. Carpenter, H. C. H. & Elam, C. F. The production of single crystals of aluminium and their tensile properties. *Proc. R. Soc. Lond. A* **100**, 329–353 (1921).
9. Zielinski, E. M., Vinci, R. P. & Bravman, J. C. The influence of strain-energy on abnormal grain-growth in copper thin-films. *Appl. Phys. Lett.* **67**, 1078–1080 (1995).
10. Zhang, J. M., Xu, K. W. & Ji, V. Strain-energy-driven abnormal grain growth in copper films on silicon substrates. *J. Cryst. Growth* **226**, 168–174 (2001).
11. Omori, T. et al. Abnormal grain growth induced by cyclic heat treatment. *Science* **341**, 1500–1502 (2013).
12. Brown, L. et al. Polycrystalline graphene with single crystalline electronic structure. *Nano Lett.* **14**, 5706–5711 (2014).
13. Xu, X. Z. et al. Ultrafast epitaxial growth of metre-sized single-crystal graphene on industrial Cu foil. *Sci. Bull.* **62**, 1074–1080 (2017).
14. Jin, S. et al. Colossal grain growth yields single-crystal metal foils by contact-free annealing. *Science* **362**, 1021–1025 (2018).
15. Kusama, T. et al. Ultra-large single crystals by abnormal grain growth. *Nat. Commun.* **8**, 354 (2017).
16. Shan, Z. W. et al. Mechanical annealing and source-limited deformation in submicrometre-diameter Ni crystals. *Nat. Mater.* **7**, 115–119 (2008).
17. Wang, H. et al. Surface monocrystallization of copper foil for fast growth of large single-crystal graphene under free molecular flow. *Adv. Mater.* **28**, 8968–8974 (2016).
18. Wang, L. et al. Epitaxial growth of a 100-square-centimetre single-crystal hexagonal boron nitride monolayer on copper. *Nature* **570**, 91–95 (2019).
19. Uecker, R. The historical development of the Czochralski method. *J. Cryst. Growth* **401**, 7–24 (2014).
20. Kelso, M. V., Tubbesing, J. Z., Chen, Q. Z. & Switzer, J. A. Epitaxial electrodeposition of chiral metal surfaces on silicon(643). *J. Am. Chem. Soc.* **140**, 15812–15819 (2018).
21. Zhang, Z. et al. Identification of copper surface index by optical contrast. *Adv. Mater. Interfaces* **5**, 1800377 (2018).
22. Ateba Betanda, Y. et al. Effect of annealing atmosphere on the recrystallized texture and abnormal grain growth of Ni-5% W alloy sheets. *Adv. Eng. Mater.* **17**, 1568–1572 (2015).
23. Dunn, C. G. & Walter, J. L. Surface energies and other surface effects relating to secondary recrystallization textures in high-purity iron, zone-refined iron, and 0.6 Pct Si-Fe. *Trans. Metall. Soc. AIME* **224**, 518–533 (1962).
24. Rhead, G. E. & McLean, M. Variation of surface energy with crystallographic orientation in silver. *Acta Metall.* **12**, 401–407 (1964).
25. McLean, M. & Mykura, H. The temperature dependence of the surface energy anisotropy of platinum. *Surf. Sci.* **5**, 466–481 (1966).
26. McLean, M. Determination of the surface energy of copper as a function of crystallographic orientation and temperature. *Acta Metall.* **19**, 387–393 (1971).
27. Ma, F., Zhang, J. M. & Xu, K. W. Surface-energy-driven abnormal grain growth in Cu and Ag films. *Appl. Surf. Sci.* **242**, 55–61 (2005).
28. Mirpuri, K. et al. Texture evolution in copper film at high temperature studied in situ by electron back-scatter diffraction. *Thin Solid Films* **496**, 703–717 (2006).
29. Na, S. M. & Flatau, A. B. Global Goss grain growth and grain boundary characteristics in magnetostrictive Galfenol sheets. *Smart Mater. Struct.* **22**, 125026 (2013).
30. Birnbaum, A. J. et al. Oxygen-induced giant grain growth in Ag films. *Appl. Phys. Lett.* **111**, 163107 (2017).

Methods

Seeded growth of single-crystal high-index Cu foils

Pre-oxidation of commercial Cu foils. A polycrystalline Cu foil (25 μm thick, 99.8%, Sichuan Oriental Stars Trading Co. Ltd, #Cu-1031) was placed on a quartz substrate and loaded into a chemical vapour deposition (CVD) furnace (Tianjin Kaiheng Co. Ltd, custom designed with a heating area of length 50 cm and diameter 23 cm). The furnace was slowly heated to 150–650 °C in 10–60 min and then maintained at this temperature for typically 1–4 h to oxidize the Cu surface.

Annealing of commercial Cu foils. The pre-oxidized Cu foil was placed on a quartz substrate and loaded into an atmospheric-pressure CVD system. The system was heated to 1,020 °C in 1 h and maintained at this temperature under a gas flow of 800 standard cubic centimetres per minute (sccm) Ar and 50 sccm H_2 for 3–10 h, and was then naturally cooled to room temperature in an Ar and H_2 atmosphere. The H_2 is necessary in the annealing process and the large single-crystal growth cannot occur in a pure Ar atmosphere.

Seeded growth of single-crystal high-index Ni foils

The Ni foils (100 μm thick, 99.994%, Alfa Aesar) were first oxidized in air at 150–650 °C for 1–4 h and then annealed in a reducing atmosphere at 1,200 °C for 3–6 h. After thermal annealing, single-crystal Ni foil of size ~5 × 5 cm^2 was successfully obtained. By repeating the typical annealing procedure, several high-index single-crystal Ni foils can be produced.

Measurement of the in-plane temperature distribution of our furnace

The temperature distribution was first simulated, as shown in Extended Data Fig. 5a. The maximum temperature difference was measured by a melting experiment using Ag foils. Nine pieces of Ag foil were placed into our furnace at different positions and were then annealed at 955 °C, 960 °C and 965 °C. With increasing temperature, different parts melted (Extended Data Fig. 5b–d), and the maximum temperature difference was estimated to be ~10 °C.

Growth of graphene and hBN

Growth of graphene. The high-index single-crystal Cu foil was placed on a quartz substrate and loaded into the CVD chamber. After heating to 1,010 °C under a reducing atmosphere (500 sccm Ar, 10 sccm H_2), CH_4 (0.5 sccm) was introduced into the system for 10–30 min. Then, the system was naturally cooled under the same reducing atmosphere. The growth was carried out under atmospheric pressure.

Growth of hBN. The as-grown single-crystal Cu foil was pre-heated and re-annealed at 1,000 °C for 30 min with a gas mixture of Ar and H_2 (500 sccm Ar, 10 sccm H_2) under atmospheric pressure. A precursor of ammonia borane was nested in a quartz crucible and heated at 65 °C for sublimation, and was then carried by Ar and H_2 (250 sccm Ar, 250 sccm H_2). To visualize the individual hBN domains, the growth time was set to be 1 h. The growth was carried out under a pressure of ~200 Pa.

Characterization

The EBSD characterizations were carried out using a PHI 710 Scanning Auger Nanoprobe instrument. LEED measurements were performed using an Omicron LEED system in ultrahigh vacuum with base pressure $<3 \times 10^{-7}$ Pa. STEM experiments were performed in a FEI Titan Themis G2 300 system operated at 300 kV. SEM images were obtained using a FEI Nova NanoSEM 430 scanning electron microscope.

XRD 2θ scan measurements were conducted using a Bruker D8 Advance system with a silver target with X-ray wavelength (~0.56 Å) shorter than that of the copper target (~1.54 Å) and more suitable for high-index facet characterization with small facet spacing. XRD φ scan measurements were conducted using a PANalytical X' Pert Pro system with a copper target. Single-crystal XRD measurements were conducted using a Bruker D8 Venture system. The primitive cell of the sample was determined by single-crystal XRD, after which the facet index of the Cu foil was obtained from the reconstructed facet that was parallel to the foil surface.

STM experiments were performed with a Createc system (Germany) under ultrahigh vacuum (~1×10^{-10} torr). To remove the contamination, the Cu foils were cleaned by Ar^+ sputtering at 1 keV and annealing at 700 K for 2–5 cycles. Then, it was transferred into the liquid-nitrogen-cooled (77 K) scanner for high-resolution imaging. All the STM images were taken at the set point of 100 mV, 50 pA. Throughout the experiments, the bias voltage refers to the sample voltage with respect to the tungsten tip.

Calculation of Cu surface energy

The surface energies of various Cu facets were obtained by density functional theory (DFT) calculations as implemented in the Vienna ab initio simulation package. The exchange-correlation effect was treated using the Perdew–Burke–Ernzerhof generalized gradient approximation. The projected augmented wave method was used to describe the interaction between valence electrons and the ionic cores. To obtain the surface energy of a certain Cu facet, a thick Cu slab consisting of ≥6 atomic layers with this facet index was constructed. In addition, a thin Cu slab, which was similar to the thick one but with only half of its atomic layers, was also fabricated. After that, both the thick and the thin Cu slabs were fully optimized via the conjugated gradient method, until the force on each atom was less than 0.01 eV $Å^{-1}$. During optimization, a vacuum slab of at least 10 Å was used to avoid the periodic imaging interaction. A separation of 0.03 $Å^{-1}$ was used for the k-point mesh sampling. The energy converged to 10^{-4} eV and an energy cut-off of 400 eV for the plane-wave basis was adopted during structure optimization. The surface energy (E) of one Cu facet can be calculated as $E = (E_{thick} - 2E_{thin})/(2A)$, where E_{thick} and E_{thin} are the energy of the thick and thin Cu slabs, respectively, and A is the area of one of the two surfaces of the slab.

Calculation on grain boundary energies

We calculated the grain boundary energies to understand the abnormal grain growth in a semiquantitative way. During the annealing process, a small grain near an abnormal grain will be transformed into a part of the abnormal grain via the propagation of the grain boundary between them (Extended Data Fig. 3d). The energy change during such a grain growth process can be estimated as $\Delta E = 2S_B(\gamma_A - \gamma_B) - (\alpha L)h\gamma_{AB}$, where $2S_B \approx 2L^2$ is the surface area of grain B (considering both sides of the metal foil); L is the lateral size of grain B; αL is the estimated length of the grain boundary between them, where $\alpha \approx 1$–4 depends on the shape of grain B (the value 4 represents a single square grain inside the abnormal grain); h is the thickness of the metal foil; γ_A, γ_B and γ_{AB} are surface energies of grain A and grain B and the grain boundary energy between grains A and B, respectively. For a thermodynamically favourable annealing process, the energy change must satisfy $\Delta E = L^2[2(\gamma_A - \gamma_B) - (\alpha\gamma_{AB}h/L)] < 0$. Obviously, if $\gamma_A - \gamma_B < 0$, this requirement will be always satisfied. However, if $\gamma_A - \gamma_B > 0$, we will have $h/L > 2(\gamma_A - \gamma_B)/(\alpha\gamma_{AB})$. For our experiment $h \approx 25$ μm, and our DFT calculations using a model of a metal slab in vacuum showed that $\gamma_B \approx \gamma_{Cu(110)} \approx 0.01$ eV $Å^{-2}$ and $\gamma_{AB} \approx 0.04$ eV $Å^{-2}$. Therefore, we have $L \approx 150$ μm when γ_A is the maximum surface energy and $\alpha = 3$. Considering that the surfaces of the Cu foil must be passivated by the hydrogen during the annealing process, the surface energy difference $\gamma_B - \gamma_{Cu(110)}$ should be much smaller than our calculated value, which is based on a model in vacuum, so we expect that the annealing of a Cu foil with much large normal grains (for example, with $L > 200$ μm) is experimentally feasible.

Molecular dynamics simulation

The calculations were performed using the software package LAMMPS (large-scale atomic/molecular massively parallel simulator). The Cu–Cu

interaction was modelled with the embedded-atom method. For seeded growth case (69,695 atoms in total), a seed ($6 \times 6 \times 1.5\ nm^3$) with in-plane orientation (345) was initially placed in the middle of the polycrystalline substrate ($16 \times 16 \times 3\ nm^3$), which was divided into 8×8 sectors with distinct orientations. The system was heated from 150 K to 1,150 K at a rate of $1\ K\ ps^{-1}$, and then annealed at 1,150 K for 20 ns. Simulations were carried out using the NVT ensemble (constant number of molecules, volume and temperature), where a Nosé–Hoover thermostat was applied to fix the temperature. The velocity Verlet algorithm was used with an integration time step of 1.0 fs. Periodical boundary conditions were applied along the x and y directions.

Data availability

All related data generated and/or analysed during the current study are available from the corresponding author on reasonable request.

Acknowledgements This work was supported by the National Natural Science Foundation of China (11888101, 51991340, 51991342, 21725302 and 51522201), National Key R&D Program of China (2016YFA0300903 and 2016YFA0300804), Beijing Natural Science Foundation (JQ19004), Beijing Excellent Talents Training Support (2017000026833ZK11), Beijing Municipal Science and Technology Commission (Z191100007219005), Beijing Graphene Innovation Program (Z181100004818003), Guangdong Provincial Science Fund for Distinguished Young Scholars (2020B1515020043), Bureau of Industry and Information Technology of Shenzhen (Graphene platform 201901161512), The Key R&D Program of Guangdong Province (2020B010189001, 2019B010931001, 2018B010109009 and 2018B030327001), Guangdong Innovative and Entrepreneurial Research Team Program (2016ZT06D348), the Science, Technology and Innovation Commission of Shenzhen Municipality (KYTDPT20181011104202253), National Equipment Program of China (ZDYZ2015-1), National Postdoctoral Program for Innovative Talents (BX201700014), China Postdoctoral Science Foundation (2018M630017 and 2019M660282) and the Institute for Basic Science of South Korea (IBS-R019-D1). We acknowledge the Electron Microscopy Laboratory in Peking University for the use of the electron microscope. K.L. acknowledges discussions with L. Lu.

Author contributions K.L. and E.W. designed and supervised the project. K.L. conceived the experiments. E.W., F.D. and K.L. developed the growth mechanism. D.Y. organized the structural characterization. M.W., Zhibin Zhang, X.X., Zhihong Zhang, L.W., J.Q., D.Z. and N.S. fabricated the single-crystal foils. F.D., H.L., Y.D. and J.D. performed the theoretical calculations. Y.J. and S.Y. performed the STM experiments. X.B., Z.-J.W., P.G., J.S., Zhibin Zhang and R.Q. performed the SEM, TEM and STEM experiments. M.W., Zhibin Zhang, X.X., Zhihong Zhang and L.Z. performed the EBSD and LEED measurements and single-crystal XRD experiments. H.Y., Y.Y. and Zhibin Zhang performed the XRD experiments with the silver target. All of the authors discussed the results and wrote the paper.

Competing interests The authors declare no competing interests.

Additional information
Correspondence and requests for materials should be addressed to F.D., D.Y., E.W. or K.L.
Peer review information *Nature* thanks Jagannathan Rajagopalan, Liu Zheng and the other, anonymous, reviewer(s) for their contribution to the peer review of this work.
Reprints and permissions information is available at http://www.nature.com/reprints.

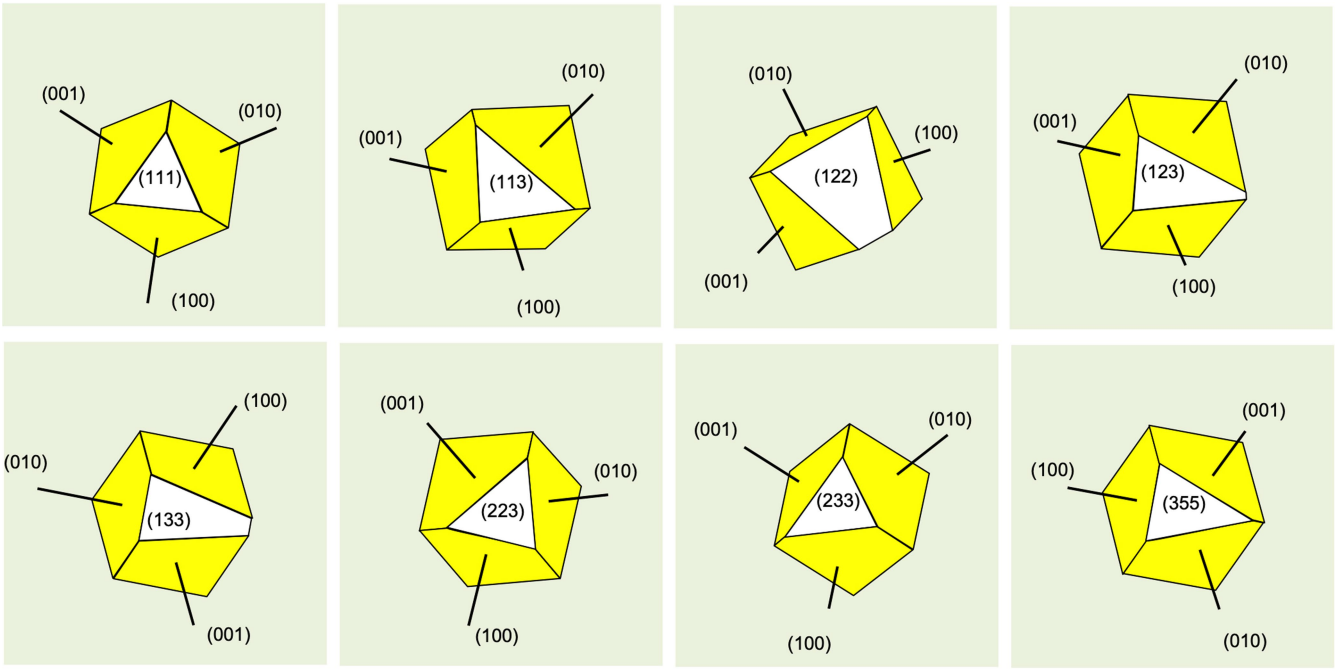

Extended Data Fig. 1 | Reconstructed single-crystal XRD images of Cu foils with various indices. Corresponding to those shown in Fig. 2. The white facets are parallel to the Cu foil surfaces.

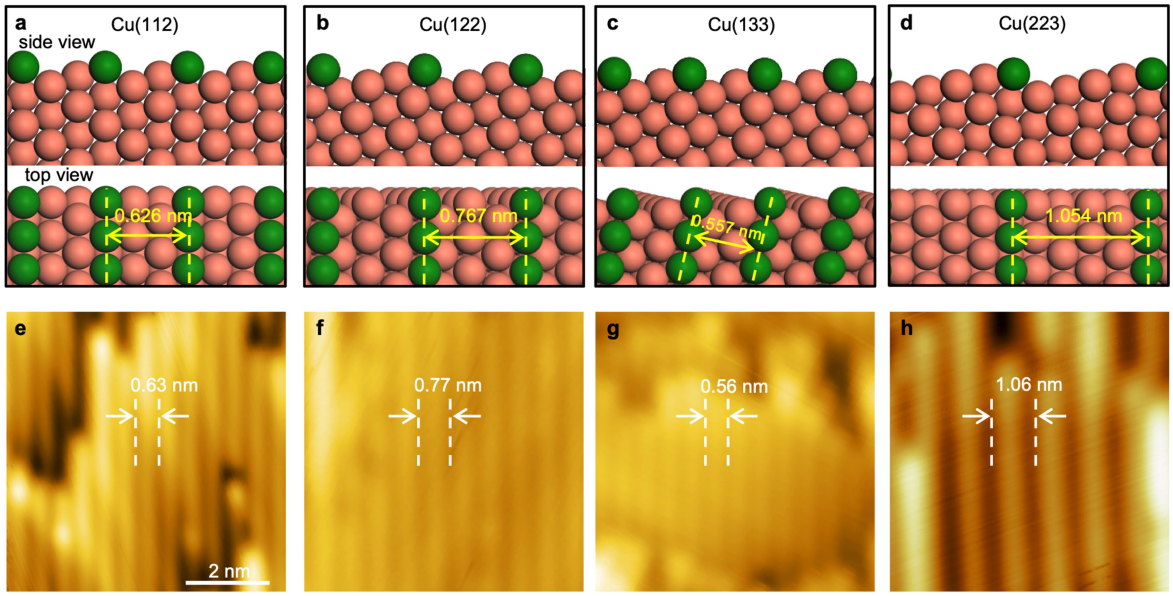

Extended Data Fig. 2 | Atomic surface structures of Cu surfaces with high-index facets. a–**d**, Atomic structures of (112) (**a**), (122) (**b**), (133) (**c**) and (223) (**d**) surfaces (top, side view; bottom, top view). **e**–**h**, Corresponding STM images of the single-crystal Cu surfaces shown in **a**–**d**. These maps are of the same size. The high-index facets feature a stripe-like structure. The measured 'stripe' spacings are consistent with calculated values from the atomic model. Because the corrugation along the Cu stripe is much smaller than that perpendicular to the stripe, owing to the strong delocalization of electrons along the stripe, the atomic resolution of Cu atoms within the stripe is not very high.

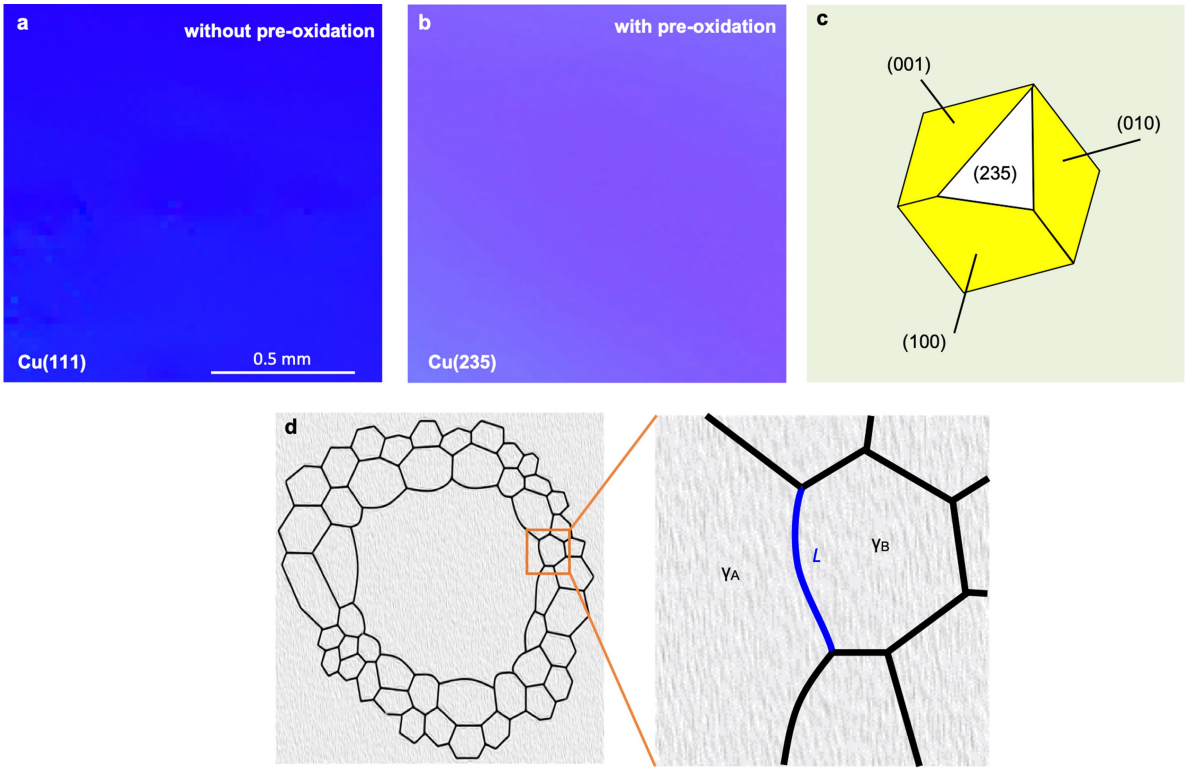

Extended Data Fig. 3 | Representative EBSD IPF maps and reconstructed single-crystal XRD image of Cu foil and the calculation model for boundary movement during abnormal grain growth. a, **b**, After annealing, the untreated terminal was transformed into Cu(111) (**a**) and the pre-oxidized part was transformed into Cu(235) (**b**). The two maps are of the same size. **c**, Reconstructed single-crystal XRD image of the Cu(235) facet. **d**, Growth of a large grain by consuming small grains around it.

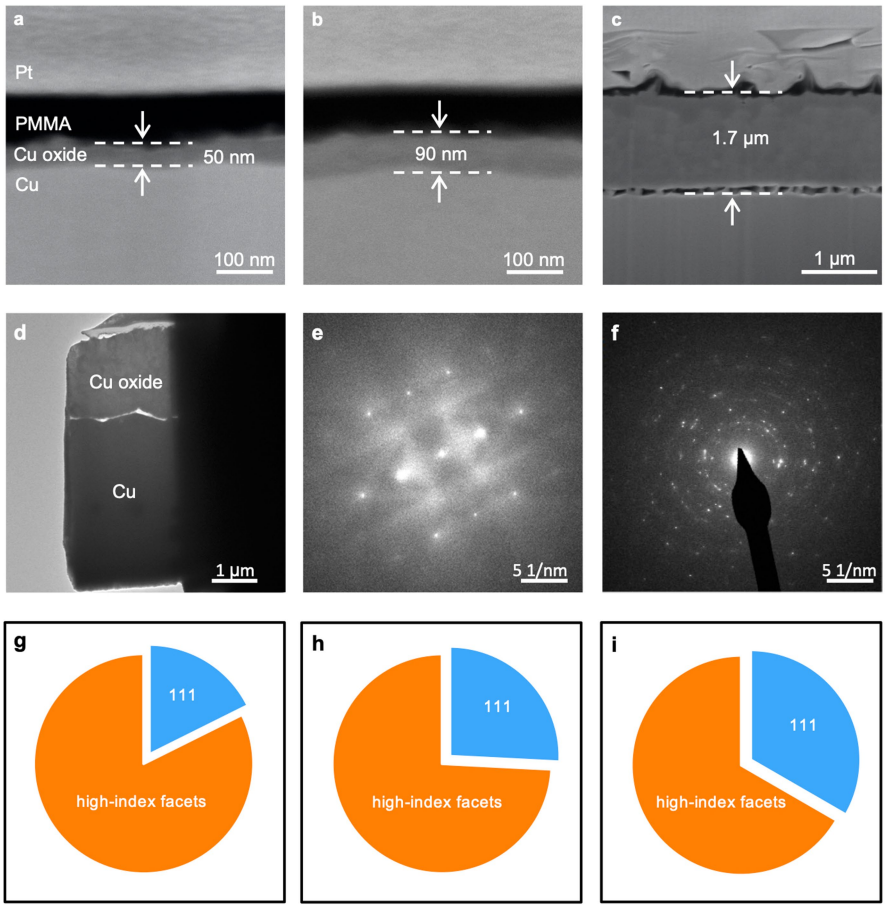

Extended Data Fig. 4 | Characterizations of the oxide layer on the Cu surface and statistics of high-index facets obtained. a–**c**, SEM images of Cu cross section after oxidation at 150 °C for 2 h (**a**), 250 °C for 2 h (**b**) and 500 °C for 1 h (**c**). The samples were prepared using the focused ion beam technique, and the polymethyl methacrylate (PMMA) and platinum (Pt) were used as protective layers to prevent damage to the sample from milling with the ion beams. **d**, Cross-sectional TEM images of Cu oxidized in air at 500 °C for 1 h. An oxidized layer was formed on the Cu surface. **e**, **f**, Selected-area electron diffraction patterns of the Cu (**e**) and the oxide layer (**f**). Unlike the single-crystal texture of the original Cu (**e**), the oxide layer has a polycrystalline structure (**f**). **g**–**i**, Statistical sector diagrams of the facet indices obtained by annealing the pre-oxidized Cu foils at conditions corresponding to **a**–**c**. The occurrence probability of high-index Cu facets was reduced from ~82% (**g**; 150 °C in air for 2 h) to ~74% (**h**; 250 °C in air for 2 h) and ~67% (**I**; 500 °C in air for 1 h), but remained very high.

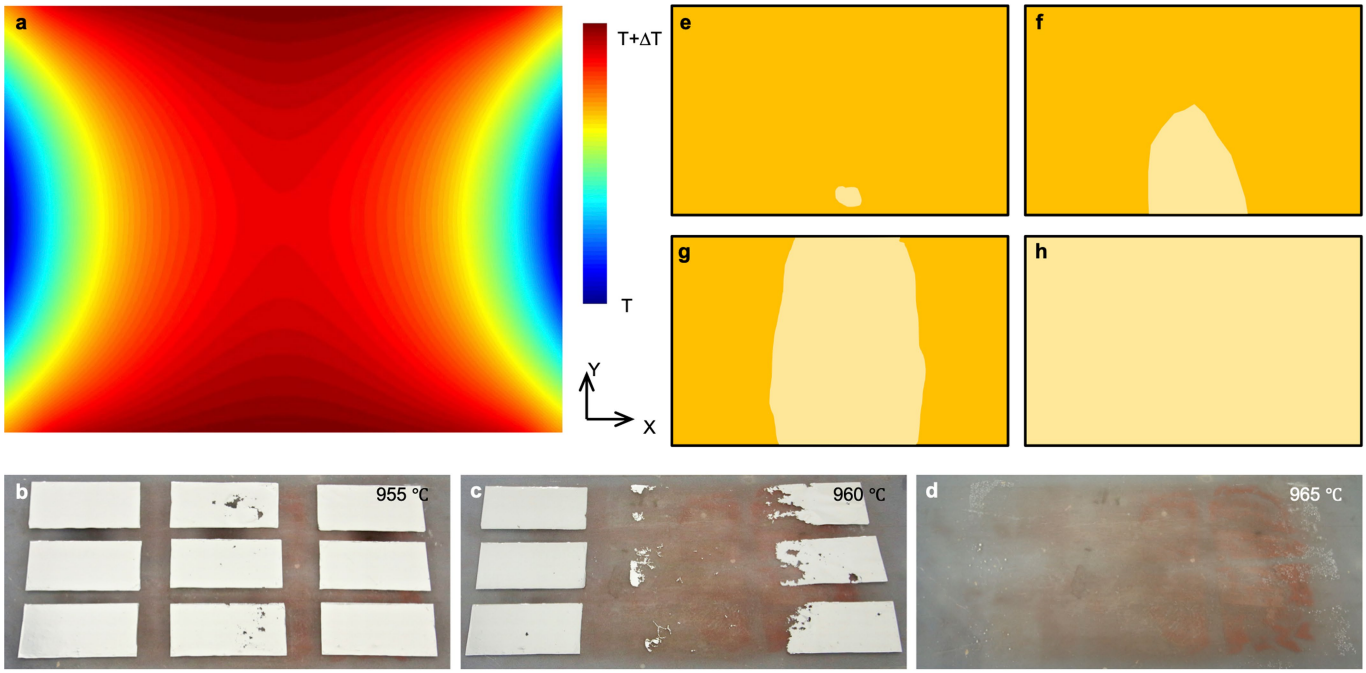

Extended Data Fig. 5 | Temperature-difference-driven single-seed abnormal grain growth. a, Simulated temperature distribution in the Cu foil. The upper and lower areas of the central part of the Cu foil have the highest temperature. **b**–**d**, Measurement of the temperature difference. Nine pieces of Ag foil were placed into our furnace and were then annealed at 955 °C (**b**), 960 °C (**c**) and 965 °C (**d**). With increasing temperature, different parts melted; the temperature difference was estimated to be ~10 °C. The image sizes for **b**–**d** are ~40 × 22 cm^2. **e**–**h**, Typical single-crystal evolution in our abnormal grain growth with a temperature difference.

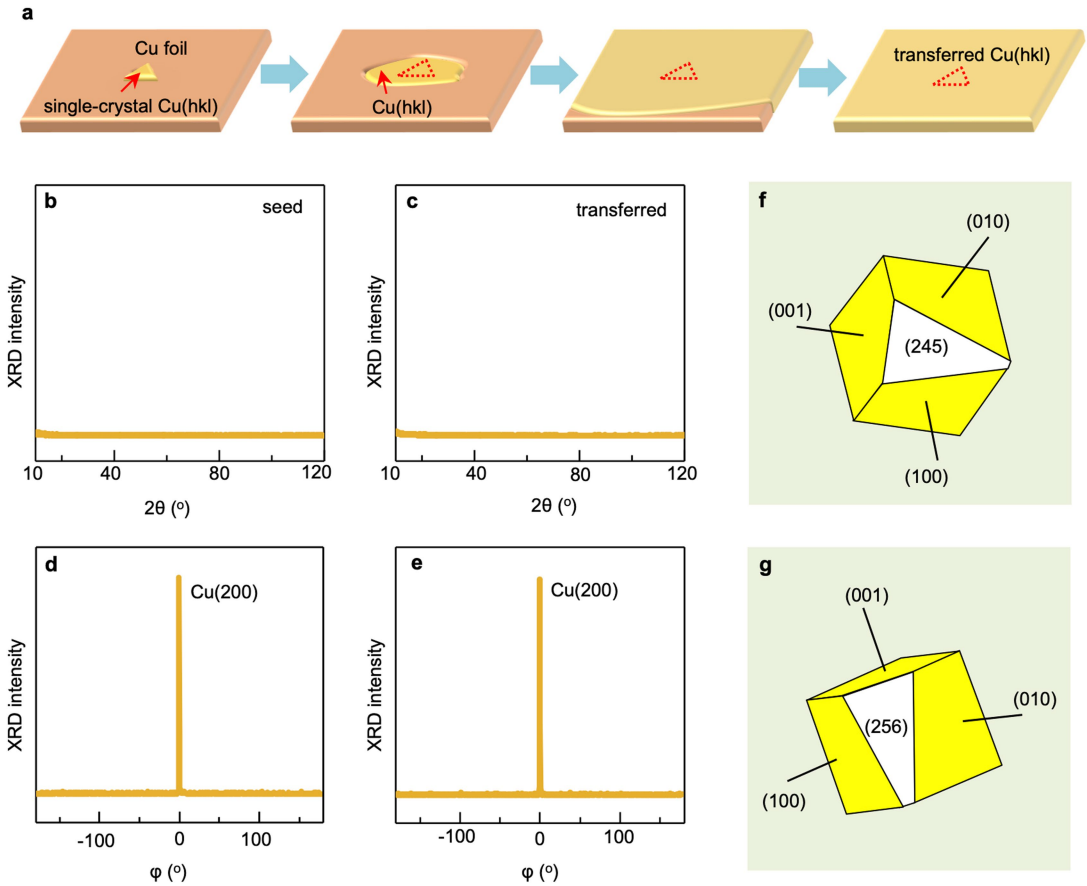

Extended Data Fig. 6 | Facet transfer and representative XRD spectra of the seed and the Cu foils with transferred facets. a, In-plane facet transfer by placing a small single-crystal Cu(*hkl*) piece on polycrystalline Cu foils. **b**–**e**, XRD 2θ (**b**) and φ (**d**) scan data for the seed, and the final Cu foil with the transferred facet (**c**, **e**). The 2θ peak for the (245) facet is out of the XRD scan range. **f**, Reconstructed single-crystal XRD image of the (245) facet, showing that the (245) seed was successfully copied and a new large-size single-crystal Cu(245) foil was produced. **g**, Reconstructed single-crystal XRD image of the Cu(256) foil.

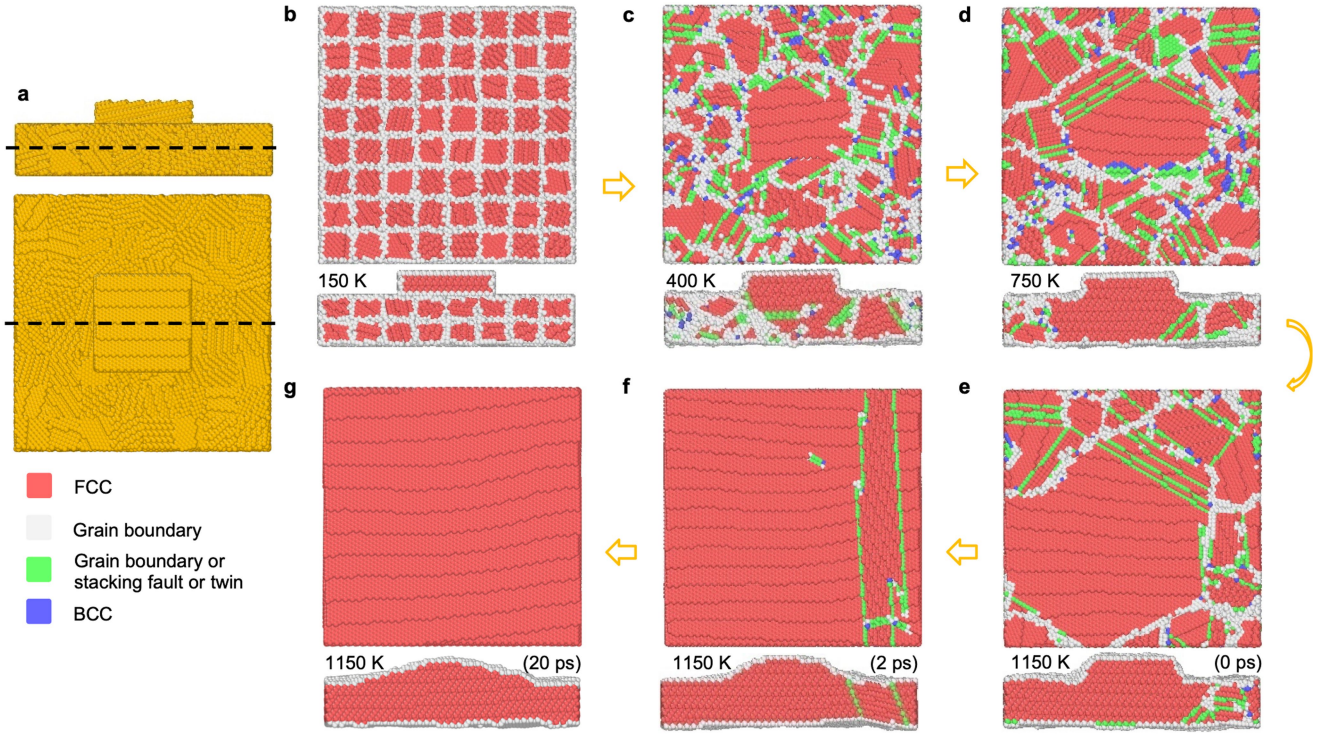

Extended Data Fig. 7 | Simulation of facet-transfer growth. a, Simulation system. **b**–**g**, Structure evolution during the heating and preservation process. Two cross-sections are presented here, marked by dark dashed lines in **a**. **b** shows the initial configuration of the system, where the substrate is composed of 64 parts with diverse in-plane orientations. The seed is placed in the middle of the substrate surface. With increasing temperature, the part of the substrate that is in contact with the seed inherits the seed orientation first; then, the seeded grain has an advantage in size over the other grains and the orientation spreads into the entire foil (**c**–**g**). Different colours in **b**–**g** indicate distinct structures, that is, the red parts have a face-centred cubic (fcc) structure; the white parts are grain boundaries; the green parts are stacking faults, twin boundaries or grain boundaries; and the blue parts have a body-centred cubic (bcc) structure.

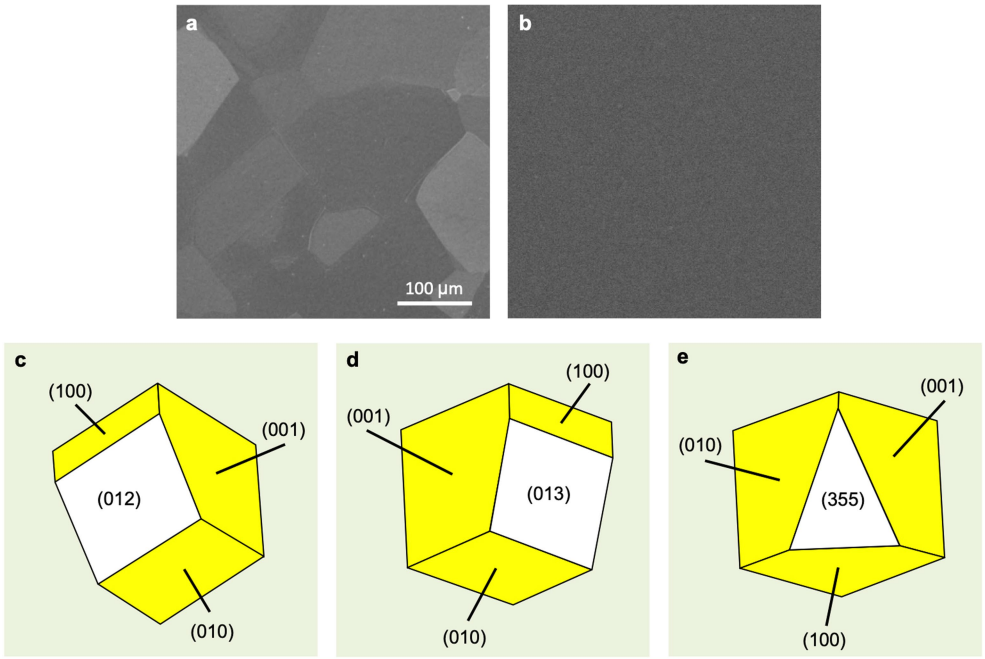

Extended Data Fig. 8 | Crystallographic characterization of high-index single-crystal Ni foils. a, **b**, SEM images of polycrystalline (**a**) and single-crystal (**b**) Ni foils with the same size. **c**–**e**, Reconstructed single-crystal XRD images of single-crystal Ni foils. The white facets are parallel to the Ni foil surfaces.

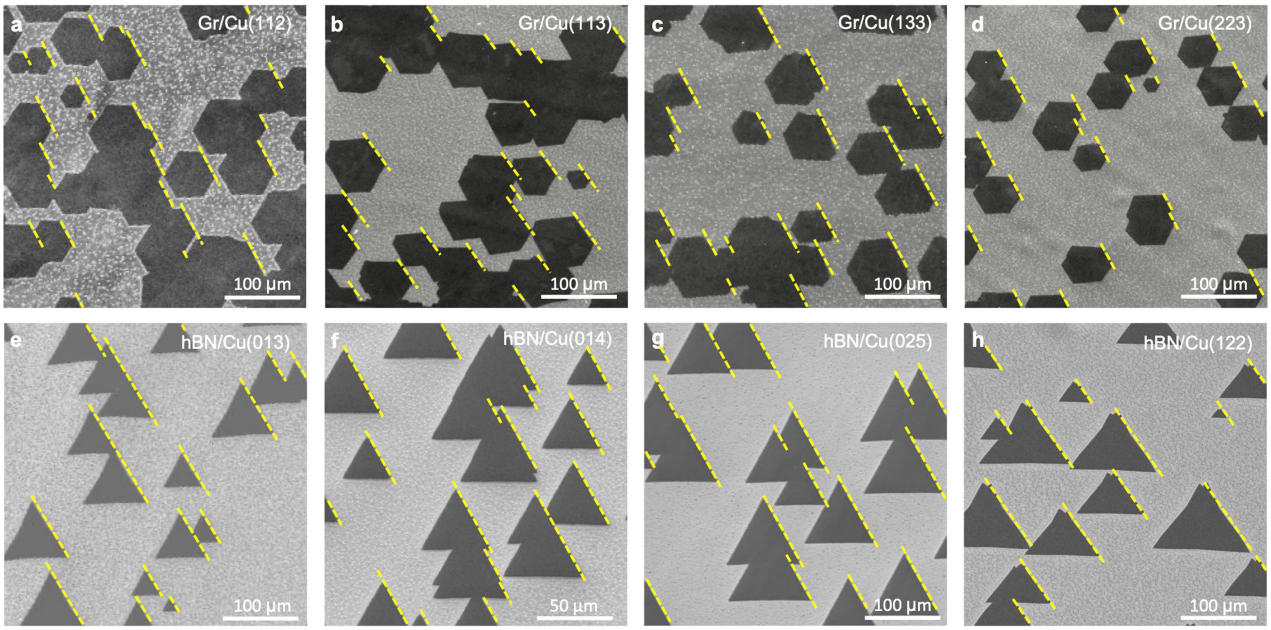

Extended Data Fig. 9 | Epitaxial growth of graphene and hBN on high-index single-crystal Cu foils. a–**d**, SEM images of unidirectionally aligned graphene (Gr) domains on (112) (**a**), (113) (**b**), (133) (**c**) and (223) (**d**) facets. **e**–**h**, SEM images of unidirectionally aligned hBN domains on (013) (**e**), (014) (**f**), (025) (**g**) and (122) (**h**) facets.

Extended Data Table 1 | Surface energy (in eV nm^{-2}) and facet characterization of single-crystal Cu foils

Facet index	011	012	013	014	023	025	034	111	112	113	115	122
Surface energy	9.90	9.91	9.92	9.79	9.86	9.95	9.74	8.10	9.40	9.60	9.30	9.20
2θ-scan XRD	√	√	√	√	√	√	√	√	√	√	√	√
Single-crystal XRD	√	√	√	√	√	√	√	√	√	√	√	√
Facet index	123	133	159	223	233	234	235	245	255	256	335	337
Surface energy	9.80	9.40	10.11	9.00	8.90	9.30	9.60	9.50	9.00	9.40	8.77	9.54
2θ-scan XRD	√	√	√	√	√	√	---	---	---	---	√	√
Single-crystal XRD	√	√	√	√	√	√	√	√	√	√	√	√
Facet index	344	345	346	355	356	357	359	377	455	456	577	
Surface energy	8.70	9.20	9.40	8.90	9.30	9.62	9.72	9.30	8.70	8.90	8.60	
2θ-scan XRD	---	---	---	√	---	√	√	√	---	---	√	
Single-crystal XRD	√	√	√	√	√	√	√	√	√	√	√	

'√' indicates that the facet index has been determined by this method, and '—' means that the corresponding 2θ peak for the facet is out of the XRD scan range.